Bioinorganic Chemistry

How to cite: *Angew. Chem. Int. Ed.* **2023,** *62,* e202209437
International Edition: doi.org/10.1002/anie.202209437
German Edition: doi.org/10.1002/ange.202209437

Spectroscopic Properties of a Biologically Relevant $[Fe_2(\mu\text{-}O)_2]$ Diamond Core Motif with a Short Iron-Iron Distance

Dustin Kass, Shenglai Yao, Konstantin B. Krause, Teresa Corona, Liza Richter, Thomas Braun, Stefan Mebs, Michael Haumann, Holger Dau, Thomas Lohmiller, Christian Limberg, Matthias Drieß, and Kallol Ray**

In memory of Dr. Eckhard Bill

Abstract: Diiron cofactors in enzymes perform diverse challenging transformations. The structures of high valent intermediates (**Q** in methane monooxygenase and **X** in ribonucleotide reductase) are debated since Fe–Fe distances of 2.5–3.4 Å were attributed to "open" or "closed" cores with bridging or terminal oxido groups. We report the crystallographic and spectroscopic characterization of a $Fe^{III}_2(\mu\text{-}O)_2$ complex (**2**) with tetrahedral (4C) centres and short Fe–Fe distance (2.52 Å), persisting in organic solutions. **2** shows a large Fe K-pre-edge intensity, which is caused by the pronounced asymmetry at the T_D Fe^{III} centres due to the short Fe–μ–O bonds. A ≈2.5 Å Fe–Fe distance is unlikely for six-coordinate sites in **Q** or **X**, but for a $Fe_2(\mu\text{-}O)_2$ core containing four-coordinate (or by possible extension five-coordinate) iron centres there may be enough flexibility to accommodate a particularly short Fe–Fe separation with intense pre-edge transition. This finding may broaden the scope of models considered for the structure of high-valent diiron intermediates formed upon O_2 activation in biology.

[*] D. Kass, K. B. Krause, Dr. T. Corona, L. Richter, Prof. Dr. T. Braun, Dr. T. Lohmiller, Prof. Dr. C. Limberg, Prof. Dr. K. Ray
Institut für Chemie, Humboldt-Universität zu Berlin
Brook-Taylor-Straße 2, 12489 Berlin (Germany)
E-mail: kallol.ray@chemie.hu-berlin.de

Dr. S. Yao, Prof. Dr. M. Drieß
Institut für Chemie, Technische Universität Berlin
Straße des 17. Juni 115, 10623 Berlin (Germany)
E-mail: matthias.driess@tu-berlin.de

Dr. S. Mebs, Dr. M. Haumann, Prof. Dr. H. Dau
Fachbereich Physik, Freie Universität Berlin
Arnimallee 14, 14195 Berlin (Germany)

Dr. T. Lohmiller
EPR4Energy Joint Lab, Department Spins in Energy Conversion and Quantum Information Science, Helmholtz Zentrum Berlin für Materialien und Energie GmbH
Albert-Einstein-Straße 16, 12489 Berlin (Germany)

Introduction

The ferritin-like dimetal-carboxylate (FDC) oxidases and oxygenases utilize a largely conserved protein structure and ligand sphere to bind nonheme dimetal cofactors that interact with dioxygen to form a variety of distinct intermediates for carrying out diverse biological functions.[1] One of the most studied FDC proteins are soluble methane monooxygenases (*s*MMO),[1a–d] which are non-heme diiron enzymes that carry out the chemically challenging conversion of methane to methanol. In presence of dioxygen the diiron active site in *s*MMO is transformed to a high-valent diiron(IV) species **Q** via the transient formation of a peroxido diiron(III) intermediate.[2] Intermediate **Q** is believed to be the key species that is able to hydroxylate the strong C–H bond of methane. Another FDC protein, class-I-a ribonucleotide[1e–i] reductases (RNRs) also contain a diiron(II/II) cofactor that reacts with oxygen to form a μ-peroxido diiron(III/III) complex, which undergoes one-electron reduction to produce the diiron(III/IV) complex, **X**.[1e,j] Intermediate **X** oxidizes a nearby tyrosine to form a stable tyrosyl radical cofactor, which serves as the initiating one-electron oxidant of cysteine to generate a thiyl radical. The latter radical mediates the conversion of ribonucleotides to deoxyribonucleotides.

In an effort to understand the process of biological methane oxidation, and reduction of ribonucleotides, numerous spectroscopic studies,[1,3] biomimetic syntheses,[4] and theoretical investigations[4a,5] have been dedicated to the elucidation of the geometric and electronic structures of the diiron intermediates **Q** and **X**. However, all these studies are yet to lead to a consensus assignment for their core structures. In particular, the discussion on the metal–metal distance, which is a key parameter that can provide insight into the core structure, is controversial. In the absence of any X-ray crystal structure of **Q**, the analysis of the extended X-ray absorption fine structure (EXAFS) previously yielded an unusually short Fe–Fe distance of 2.46 Å, which might be accommodated by a closed-shell $Fe_2(\mu\text{-}O)_2$ "diamond-core" structure (Scheme 1).[3c] Similarly short Fe–Fe distances (≈2.5 Å) were also tentatively suggested for RNR cofactors.[6a,b] However, such assignments were questioned and the short distance was attributed to metallic iron contributions.[3a,b,5f,6c] So far, neither computational nor

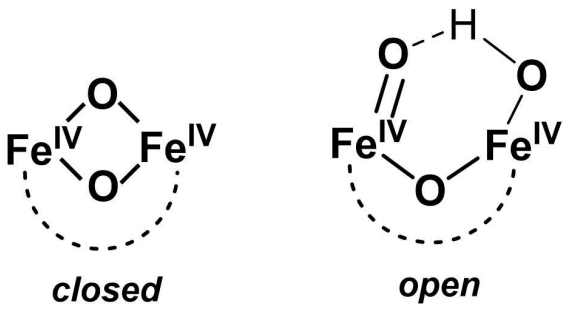

Scheme 1. Proposed closed and open forms for the structure of **Q** (the dashed line represents the protein backbone in the enzyme). Spectroscopic characterizations of synthetic model complexes of both the forms have been reported.[3b,e,10]

synthetic efforts could successfully reproduce such a short Fe–Fe distance in a "closed" $Fe_2(\mu\text{-}O)_2$ diamond core. In fact, analysis of the recent high energy resolution fluorescence detected (HERFD) EXAFS data of **Q** reveals a longer Fe–Fe separation of ≈3.4 Å.[3b] This finding, together with the large pre-edge intensity observed in the HERFD X-ray absorption spectrum (XAS) spectrum of **Q** led DeBeer and co-workers[3a,b] to favour a diiron core of significantly decreased symmetry and large covalent contributions in **Q**, as might be provided by an "open core" conformation with terminal oxido ligand(s). However, recent studies of **Q** reported by Solomon and co-workers,[3e] employing nuclear resonance vibrational spectroscopy, favour a closed-core description for this intriguing intermediate. Similarly, for **X**, the recent electron nuclear double resonance (ENDOR) experiments[3j] suggest that it might also have an "open core" structure with only a single nonprotein oxygen bridge. However, this conclusion is potentially incompatible with the Fe–Fe distance of 2.8 Å determined by EXAFS for **X**,[6c] which is comparable to the Fe–Mn distance of 2.75 Å noted for the "closed" $Mn^{IV}(\mu\text{-}O)_2Fe^{IV}$ diamond core[3j] in class 1-c RNRs. Thus, although the structures of these intermediates are of significant interest, their definition is still controversial.

The two most discussed examples of synthetic complexes with $Fe_2(\mu\text{-}O)_2$ diamond cores characterized by X-ray diffraction (XRD) analyses known to date, namely $[Fe^{III}_2(\mu\text{-}O)_2(6\text{-}Me_3TPA)_2]^{2+}$[7] and $[Fe^{III}Fe^{IV}(\mu\text{-}O)_2(5\text{-}Et_3TPA)_2]^{3+}$,[8] both exhibit Fe–Fe separations of ≈2.7 Å. Notably, a Fe–Fe distance of 2.71 Å is also determined for a $[Fe^{IV}_2(\mu\text{-}O)_2(TPA^*)_2]^{3+}$ complex.[3f,9] Comparison of these three examples suggests that the Fe oxidation states may have only little influence on the Fe–Fe separation in $Fe_2(\mu\text{-}O)_2$ diamond cores. By contrast, an unexpected reduction of the Fe–Fe distance by 0.11 Å was observed to occur upon one-electron reduction of the recently reported complex $[Fe^{IV}_2(\mu\text{-}O)_2(TPA^*)_2]^{2+}$ to give $[Fe^{III}Fe^{IV}(\mu\text{-}O)_2(TPA^*)_2]^{2+}$,[3f] this has been attributed to differences in the spin-coupling between the two iron centres in the two complexes. The consensus from all the synthesis, theoretical, and XAS studies is that a Fe–Fe distance of ≈2.7–2.8 Å and a diminished pre-edge intensity is more representative of a diamond core structure containing 6-coordinate iron atoms. Conversely, an increased pre-edge transition would warrant an asymmetric open-core $O{=}Fe^{IV}{-}O{-}Fe^{IV}$ conformation containing 6C Fe and a terminal oxidoiron(IV) motif (Scheme 1).[10] An inherent question is now, whether a large Fe K-pre-edge intensity can be also accommodated within a closed $Fe_2(\mu\text{-}O)_2$ diamond core containing lower coordinated iron centres, as has been suggested in few theoretical studies for intermediate **Q**.[3a,b,e]

In our effort to examine the effects of diminished coordination numbers at the iron site on the Fe–Fe separation in $Fe_2(\mu\text{-}O)_2$ diamond cores, we have employed sterically demanding β-diketiminato ligands, which have been previously used by us and others for the synthesis of bioinspired reactive intermediates relevant to nitrogenases, [NiFe]-hydrogenases and various oxygenases.[13] We now report the X-ray structure of a $[Fe_2(\mu\text{-}O)_2(L)_2]$ (L = CH-[CMeN(2,6-$Et_2C_6H_3$)]$_2$) (**2**) complex containing 4-coordinate iron(III) ions in tetrahedral geometry. Complex **2** exhibits a Fe–Fe separation of 2.53 Å, which is at the lower end of the proposed range of iron separations suggested for **X** and **Q**. The X-ray absorption near-edge spectrum (XANES) of **2** shows a large pre-edge intensity (Figure 2). Furthermore, **2** represents a rare example of an O_2 derived $Fe_2(\mu\text{-}O)_2$ diamond core, which reproduces some of the spectroscopic features of **Q**, despite being two-electrons more reduced.

Results and Discussion

Reaction of the previously reported complex $[L_2Fe_2(\mu\text{-}H)_2]$ (**1**)[14] (where L is the bulky β-diketiminato ligand in Scheme 2) with O_2 in tetrahydrofuran (THF) or toluene at −90 °C gives red-brown $[L_2Fe_2(\mu\text{-}O)_2]$ (**2**) in near-quantitative yield. The conversion of **1** to **2** can be followed by UV/Vis absorption spectroscopy. Bubbling of O_2 at −80 °C to a toluene solution of **1** leads to the appearance of two new bands at 410 nm (ε_{max} = 1300 $M^{-1}cm^{-1}$) and 550 nm (ε_{max} = 1300 $M^{-1}cm^{-1}$) corresponding to **2** (Figure S1). We suggest a mechanism, whereby **1** acts as a masked Fe^I precursor; **1** undergoes H_2 elimination to generate the transient dinuclear $[LFe^I]_2$ complex, which activates O_2 to form **2**. Notably, similar intramolecular reductive H_2 elimination reactions have been noted previously in a series of dinuclear nickel β-diketiminato complexes.[13c,d] The attenuated total reflection

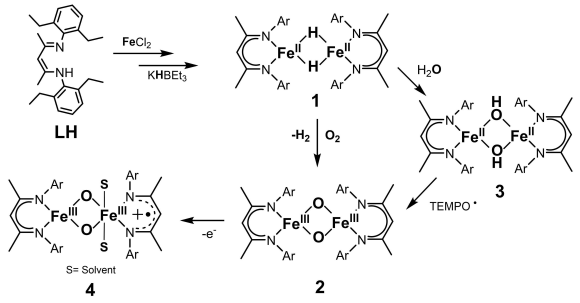

Scheme 2. Synthesis of the complexes **2–4**.

Fourier-transform infrared (ATR-FTIR) spectroscopy corroborates the incorporation of both oxygen atoms of O_2 in **2**, consistent with this mechanism. In the ATR-FTIR spectrum (Figure 1C), two prominent bands at 561 cm^{-1} and 590 cm^{-1} are shifted to lower energies by 26 cm^{-1} and 25 cm^{-1}, respectively, when employing $^{18}O_2$ in the synthesis of **2**. According to the density functional theory calculations (DFT) (Figure S2), these bands correspond to the asymmetric and symmetric "breathing" modes, respectively, of the $[Fe_2(\mu\text{-}O)_2]$ diamond core in **2** and are calculated at 570 cm^{-1} and 595 cm^{-1}, respectively.

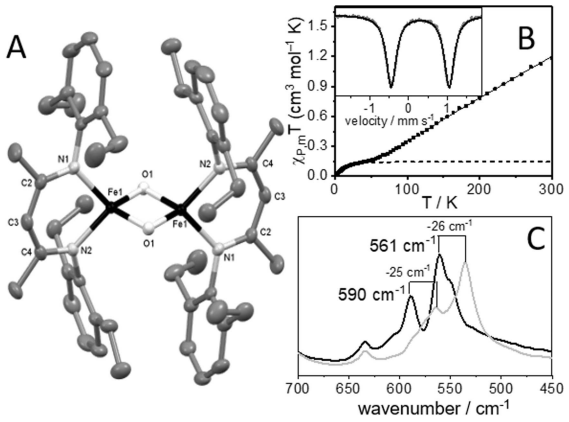

Figure 1. A) Molecular structure of **2** (hydrogens and a crystalized toluene omitted for clarity; Fe black, O light grey, N grey, C dark grey).[17] Thermal ellipsoids are drawn at 50% probability level. B) Molar paramagnetic susceptibility data for **2** (dots) recorded at 7 T, plotted as $\chi_{p,m}T$ vs. *T*. The overall fit to the data is plotted as a solid line, while the 3.3% paramagnetic impurity is plotted as a dashed line. Inset: Zero field Mössbauer spectra at 15 K of **2** ($\delta = 0.30$ mm s^{-1}, $\Delta E_Q = 1.50$ mm s^{-1}, 98%). C) ATR-FTIR spectra of solid **2** (black) and ^{18}O-labelled **2** (grey).

Table 1: Comparison of the most important bond lengths of the complexes (averaged distances, in Å). For the DFT calculated structure of **2** see Figure S18.

	2 (XAS)	**2** (XRD)	**2** (DFT)	**3** (XRD)[17]	**3** (XAS)	**4** (XAS)
Fe–Fe	2.51	2.53	2.54	3.06	3.04	2.91
Fe–O	1.81	1.85	1.84	1.99 2.03	1.97	1.76
Fe–N	1.97	2.01	2.00	2.06	2.05	2.01

The same compound **2** can also be accessed in quantitative yield by adding two equivalents of TEMPO (2,2,6,6-tetramethylpiperidin-1-oxyl) to the $[L_2Fe^{II}_2(\mu\text{-}OH)_2]$ complex **3** (Scheme 2 and Figure S3), which, in turn, is generated by the reaction of **1** with H_2O (for molecular structure see Figure S4 and for ^{57}Fe-Mössbauer spectrum see Figure S5A). The molecular structure of **2**, shown in Figure 1A and Figure S6, consists of a centrosymmetric $[Fe_2(\mu\text{-}O)_2]$ rhomb with the two nitrogen atoms of the β-diketiminato ligand completing the distorted tetrahedral environment of each iron centre. Complex **2** represents a rare example of a crystallographically characterized $[Fe_2(\mu\text{-}O)_2]$ diamond core structure containing four-coordinate Fe centres,[12] and it exhibits some unique structural features compared to those of the previously reported $[Fe^{III}_2(\mu\text{-}O)_2(6\text{-}Me_3TPA)_2]^{2+}$,[7] $[Fe^{III}Fe^{IV}(\mu\text{-}O)_2(5\text{-}Et_3TPA)_2]^{3+}$,[8] $[Fe^{III}Fe^{IV}(\mu\text{-}O)_2(TPA^*)_2]^{3+}$, and $[Fe^{IV}Fe^{IV}(\mu\text{-}O)_2(TPA^*)_2]^{3+}$ complexes. Firstly, the Fe–Fe distance decreases dramatically from 3.06(3) Å in **3** to 2.5269(4) Å in **2** (Table 1). The latter distance is comparable to the Fe–Fe distance of 2.46 Å reported in the initial EXAFS analysis of intermediate **Q**,[3c] which is now attributed to arise from metallic iron contributions.[3b] Secondly, the Fe–O–Fe angle of 86.43(5)° is one of the smallest values for synthetic $[Fe_2(\mu\text{-}O)_2]$ motifs and may reflect increased repulsion between the two oxido bridges. Notably, the average Fe–O distance of 1.85 Å for **2** is comparable to the Fe–O distance of intermediate **Q** (Table 2).[3c]

X-ray absorption spectroscopy provides insights into the redox state and coordination geometry of the iron complexes (Figure 2, Table 1, Figures S7–S12, Tables S1–S5). The K-edge energy of **2** at 7123.3 ± 0.2 eV suggests two Fe^{III} centres, which is in contrast to the one of **3** (7119.7 eV) containing two Fe^{II} centres.

Table 2: Comparison of the main structural and spectroscopic features of intermediate **Q** and **2**.

	Intermediate **Q**	**2**
Fe–O vibration(s)	556 cm^{-1}, 690 cm^{-1} [3d]	561 cm^{-1}, 590 cm^{-1}
Fe–O distance	1.85 Å[3c]	1.8571(12) Å 1.8332(11) Å
Fe–Fe distance	2.46 Å,[3c][a] ≈3.4 Å,[3b][b] 2.69–3.0 Å[3e][c]	2.5269(4) Å 2.50(2) Å[a]
Fe K-edge energy	7126.2 eV[3b][b,d]	7123.3(0.2) eV[a]
Fe pre-edge energy	7114.0 eV[3b][b,d]	7114.3(0.2) eV[a]
Fe pre-edge area	42[3a][b] 28[3c][a]	41(3)[a]
UV/Vis absorption	430 nm[3d]	415 nm, 530 nm
Mössbauer	$\delta = 0.17$ mm s^{-1}, $\Delta E_Q = 0.53$ mm s^{-1}	$\delta = 0.30$ mm s^{-1}, $\Delta E_Q = 1.50$ mm s^{-1}

[a] XAS with a calibration energy of 7112.0 eV; [b] HERFD XAS with a calibration energy of 7111.2 eV; [c] NRVS; [d] We note that comparison of pre/K-edge parameters from conventional or HERFD XAS may be limited due to spectral shape changes.

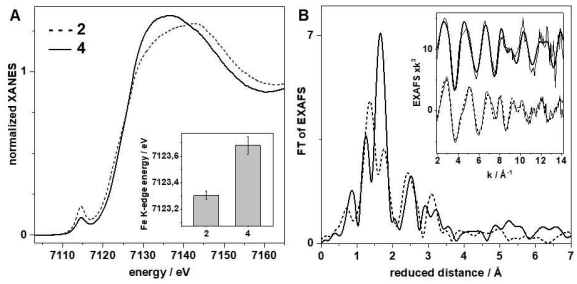

Figure 2. XAS spectra of **2** and **4**. A) XANES spectra (K-edge energies in the inset). B) Fourier-transforms of the k-space EXAFS spectra as shown in the inset (grey lines, experimental data; black lines, simulations). See Figures S7–S12 and Tables S1–S5 for simulation parameters and further XAS data.

Analysis of the extended X-ray absorption fine structure (EXAFS) data of **2** in powder and acetonitrile (CH_3CN) solution samples yields similar metrical parameters, which are in good agreement with the crystal data for **2** (Table 1, Figure S7). Also, the EXAFS data of **3** with di-μ_2-hydroxido bridged Fe^{II} centres comply well with the molecular structure. The best-fit results for **2** comprise two oxygen ligands at 1.81 ± 0.02 Å, which are assigned to the [$Fe_2(\mu\text{-}O)_2$] unit, as well as two nitrogen donors at 1.97 ± 0.02 Å, belonging to the β-diketiminato ligands. An additional Fe scatterer at 2.50 ± 0.02 Å is needed for a good simulation of the experimental spectra, thereby showing that the dinuclear structure with an exceptionally short Fe–Fe distance is also largely maintained in solution. Notably, for **2** in CH_3CN solution an EXAFS contribution of a second species with longer Fe–Fe distance (≈3.0 Å, Tables S2 and S5) was increased at the expense of the ≈2.5 Å distance of **2**, suggesting limited formation of a more oxidized form of the complex (as characterized further below).[15] A small contribution from the species with a ≈3 Å Fe–Fe distance may also be present already in the powder material of **2** (Tables S2 and S5) as suggested also by the relatively large Debye–Waller factor of the short Fe–Fe distance (Table S1). Notably, also small metallic iron background contributions may not be fully excluded for the dilute solution samples, which may diminish the visual contributions of the Fe–Fe distances to the FT EXAFS spectra due to interference effects.[15] Similar EXAFS properties were found for **2** in butyronitrile and acetone solutions but increasing amounts of species with ≈3.5 Å Fe–Fe distances were detected, possibly reflecting the formation of degradation products such as iron-oxides (data not shown). The Fe K-edge of **2** features an intense pre-edge feature at ≈7114.3 eV, which is due to the pronounced asymmetry in bond lengths at the near-tetrahedral iron centre. Its intensity in powder and various organic-solvent samples (Figure S9, Table S3) is comparable to that observed for **Q** in HERFD XAS spectra (Table 2).[3a,15]

The zero-field Mössbauer spectrum of **2** (Figure 1B inset) shows a single quadruple doublet with an isomer shift $\delta = 0.30\ mm\,s^{-1}$ and a quadrupole splitting $\Delta E_Q = 1.50\ mm\,s^{-1}$, which is considerably different from that in **Q** with $\delta = 0.17\ mm\,s^{-1}$ and $\Delta E_Q = 0.53\ mm\,s^{-1}$, respectively.[15] These values are consistent with the presence of high-spin Fe^{III} centres in **2** so that it is two equivalents less oxidized compared to **Q**. Molar paramagnetic susceptibility data for **2** and spin-Hamiltonian-based simulations thereof are plotted in Figure 1B. The value for $\chi_{p,m}T$ decreases approximately linearly with temperature from $1.19\ cm^3\,mol^{-1}\,K$ at 300 K to $0.23\ cm^3\,mol^{-1}\,K$ at 73 K, indicative of antiferromagnetic interaction of the Fe^{III} spins. Further lowering of the temperature results in a nonlinear, less steep decrease, reaching $0.09\ cm^3\,mol^{-1}\,K$ at 14 K. The temperature range of this levelling of the linear decrease is determined by the coupling strength and allows for fitting of *J*. The fact that $\chi_{p,m}T$ does not converge slowly towards zero, but instead drops again more rapidly from ≈14 K towards $0.02\ cm^3\,mol^{-1}\,K$ at 2 K is due to the presence of a small percentage of paramagnetic impurity (see Supporting Information for details). The simulation yields optimized parameters $g = 2.052$ and $J = -97\ cm^{-1}$. While the slight deviation of the *g*-value from the free electron value of 2.002 is likely due to imperfect measurement of the sample mass, the coupling constant *J* is nonetheless very accurate, as the curvature that it defines is unaffected.

Because **2** is more reduced relative to intermediates **X** and **Q**, we explored the electrochemistry of **2** to oxidize it to the mixed valent $Fe^{III}Fe^{IV}$ and $Fe^{IV}Fe^{IV}$ forms. In cyclovoltammetric studies (Figure S13), scanning anodically from 0 V versus the ferrocenium/ferrocene couple ($Fc^{+/0}$) elicits an oxidative wave with a peak potential $E_{p,a} = +0.72$ V versus $Fc^{+/0}$ for **2** in CH_3CN at room temperature; scan reversal below −0.5 V gives rise to a reductive wave with a peak potential $E_{p,c} = -0.47$ V, which is not observed unless the oxidative wave at +0.72 V is also present. Although not strictly reversible according to CV criteria, the oxidation of **2** to the one-electron oxidized species **4** could be achieved by spectropotentiometric and chemical methods. In UV/Vis spectroelectrochemistry, the oxidation wave at +0.72 V is associated with a decrease in intensity of the characteristic feature of **2** at 415 nm and increasing intensity of absorption features at 470 nm and 690 nm (Figures S14 and S15). Similar changes were also observed during the chemical oxidation of **2** to **4** in presence of $NO^+SbF_6^-$ as an oxidant ($E = +0.87$ V vs $Fc^{+/0}$ in CH_3CN). Titration experiments with different amounts of $NO^+SbF_6^-$ showed that exactly one equivalent of oxidant is required for achieving maximum intensity at 690 nm, thereby confirming **4** as the one-electron oxidation product of **2** (Figure 3A inset and Figure S16).

While **2** is silent in X-band electron paramagnetic resonance (EPR) spectroscopy, the formation of **4** is associated with the generation of a signal at $g = 4.3$ corresponding to the $S = 5/2$ ground state of **4** (Figure 3B inset and Figure S17). ^{57}Fe Mössbauer spectroscopy demonstrates that the oxidation occurs at the β-diketiminato ligand, rather than at the iron atoms. The spectra of **4** in a frozen acetone/CH_3CN 10/1 solution can be well fit with two overlapping quadrupole doublets in 1:1 ratio, formally representing the locally high-spin Fe^{III} ($\delta = 0.31\ mm\,s^{-1}$, $\Delta E_Q = 1.33\ mm\,s^{-1}$) and low-spin Fe^{III} ($\delta = 0.46\ mm\,s^{-1}$,

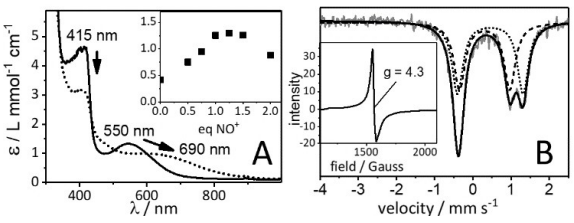

Figure 3. A) UV/Vis Spectral changes associated with the conversion of **2** (bold line) to **4** (dotted line) in presence of $NO^+SbF_6^-$ as an oxidant. The inset shows the spectral titration experiment revealing that approximately 1 equiv of $NO^+SbF_6^-$ is required for achieving maximum intensity of the 690 nm band corresponding to **4**; more than 1 equiv of $NO^+SbF_6^-$ leads to a decay of **4**. B) The Mössbauer spectrum recorded on a frozen acetone/CH_3CN 10/1 solution of **4** (bold) at 12 K with the simulation of two subspecies (sub1: $\delta = 0.31$ mm s^{-1}, $\Delta E_Q = 1.33$ mm s^{-1}, 50% dashed line; sub2: $\delta = 0.46$ mm s^{-1}, $\Delta E_Q = 1.72$ mm s^{-1}, 50%, dotted line). The inset shows the X-band EPR spectrum of **4** in frozen acetone/CH_3CN 10/1 solution at 5 K.

$\Delta E_Q = 1.72$ mm s^{-1}) centres.[16] In contrast to the four-coordinated tetrahedral high-spin Fe^{III} site, the low-spin Fe^{III} centre, which is attached to the oxidized β-diketiminato ligand ($L^{+\bullet}$) is presumably five- or six-coordinated with additional CH_3CN donors. This is also evident from ESI-MS data, which shows a peak at $m/z = 907.5$ (Figure S18) that can be assigned to a $[Fe_2O_2L_2(CH_3CN)]^+$ species. The $S = 1/2$ low-spin Fe^{III} centre must be coupled antiferromagnetically to $L^{+\bullet}$ giving a total-spin of $S = 5/2$ for the $[(L)Fe^{III}O_2Fe^{III}(L^{+\bullet})(CH_3CN)]^+$ core in **4**, as evident from the $g = 4.3$ signal in the X-band EPR spectrum. Additional binding of solvent(s) is also visible in the XANES spectrum of **4**, which reveals an increased primary maximum and diminished pre-edge amplitude relative to the spectrum of **2** (Figure 2, Figure S9). These features are indicative of a more centro-symmetric coordination at the iron centres in **4** compared to **2**. Qualitatively similar but less pronounced XANES changes were detected for oxidation of **2** in butyronitrile or acetone solutions (not shown). Indeed, EXAFS analysis of **2** in CH_3CN (and less pronouncedly in butyronitrile or acetone) after oxidation by addition of $NO^+SbF_6^-$ revealed an increased 1st-sphere coordination number of 5–6, as evident from the pronouncedly increased main Fourier-transform peak (Figure 2), as well as rising contributions of a longer Fe–Fe distance of ≈3 Å due to increasing concentrations of **4** (Figures S11, S12, Tables S4 and S5). However, the K-edge energy increased only slightly (≈0.4 eV) relative to the value obtained for **2** (Figures 2 and S10), further corroborating the ligand-based oxidation in **4**.

Conclusion

In summary, we report the synthesis and characterization of an O_2-derived four-coordinate $[Fe_2(\mu\text{-}O)_2]^{2+}$ complex **2** and show that lower coordination number for the irons allows much more flexibility in the diamond core than proposed based on many other computational and experimental studies. Notably, the concept of building in flexibility by diminishing the metal coordination number has broader mechanistic significance because such changes within enzyme reaction cycles are used often by nature to drive respective catalysis. Furthermore, comparison (Tables 2 and S9 in Supporting Information) of the XANES data of the "closed" $Fe^{III}{}_2(\mu\text{-}O)_2$ core motif of **2** with a short Fe–Fe separation of 2.53 Å and the values for **Q** and for a synthetic higher-valent open core $(OH)Fe^{IV}\text{–}O\text{–}Fe^{IV}(O)$ complex[10] with a larger Fe–Fe distance of 3.32 Å reveals that their pre-edge energies and intensities may reach similar values. The large pre-edge intensity of **2** can be plausibly attributed to enhanced p/d-mixing in a four-coordinate T_d iron site with considerable asymmetry due to short Fe–μ–O bonds, facilitating dipole-forbidden 1s→3d electronic transitions. Whether such a phenomenon in a $[Fe^{IV}{}_2(\mu\text{-}O)_2]^{2+}$ diamond core motif, where at least one of the Fe centres is five-coordinate, as suggested in recent theoretical studies,[3b,e] could also account for the resonant X-ray absorption features of **Q** is a particularly intriguing question, which should be verified in future studies. Oxidation of complex **2** leads to the oxidation of the ligand instead of the metal, generating a novel example of a diiron(III) complex, **4**, containing a non-innocent β-diketiminato ligand.

Acknowledgements

This work was funded by the Deutsche Forschungsgemeinschaft (DFG, German Research Foundation) under Germany's Excellence Strategy—EXC 2008-390540038—UniSysCat to D.K., K.R., K.K., T.B., M.D., C.L., M.H., and H.D., and the Heisenberg-Professorship to K.R. T.C. thanks the Alexander von Humboldt Foundation for their support. H.D. and M.H. acknowledge support by the BMBF in the Operando-XAS project (Grant no. 05K19KE1). We acknowledge the Helmholtz Zentrum Berlin (HZB) for providing experimental infrastructure and allocating beamtime at beamline KMC-3 of the BESSY synchrotron and thank Ivo Zizak and further BESSY staff for their support. T.L. acknowledges support by the DFG (Project No. LO 2898/1-1). Open Access funding enabled and organized by Projekt DEAL.

Conflict of Interest

The authors declare no conflict of interest.

Data Availability Statement

The data that support the findings of this study are available from the corresponding author upon reasonable request.

Keywords: Bioinorganic Chemistry · Diamond Core · Intermediate **Q** · Iron Cofactors · Soluble Methane Monooxygenase

[1] a) B. Battistella, K. Ray, *Coord. Chem. Rev.* **2020**, *408*, 213176–213191; b) R. S. Hanson, T. E. Hanson, *Microbiol. Rev.* **1996**, *60*, 439–471; c) M. O. Ross, A. C. Rosenzweig, *J. Biol. Inorg. Chem.* **2017**, *22*, 307–319; d) R. Banerjee, J. C. Jones, J. D. Lipscomb, *Annu. Rev. Biochem.* **2019**, *88*, 409–431; e) B. E. Sturgeon, D. Burdi, S. Chen, B.-H. Huynh, D. E. Edmondson, J. Stubbe, B. M. Hoffman, *J. Am. Chem. Soc.* **1996**, *118*, 7551; f) J. Stubbe, W. A. van der Donk, *Chem. Rev.* **1998**, *98*, 705–762; g) W. Jiang, D. Yun, L. Saleh, E. W. Barr, G. Xing, L. M. Hoffart, M.-A. Maslak, C. Krebs, J. M. Bollinger, Jr., *Science* **2007**, *316*, 1188–1191; h) J. A. Cotruvo, Jr., T. A. Stich, R. D. Britt, J. Stubbe, *J. Am. Chem. Soc.* **2013**, *135*, 4027–4039; i) J. Stubbe, D. G. Nocera, C. S. Yee, M. C. Y. Chang, *Chem. Rev.* **2003**, *103*, 2167–2202; j) D. Burdi, B. E. Sturgeon, W. H. Tong, J. Stubbe, B. M. Hoffman, *J. Am. Chem. Soc.* **1996**, *118*, 281–282; k) W. Jiang, J. M. Bollinger, Jr., C. Krebs, *J. Am. Chem. Soc.* **2007**, *129*, 7504–7505.

[2] a) C. E. Tinberg, S. J. Lippard, *Acc. Chem. Res.* **2011**, *44*, 280–288; b) A. C. Rosenzweig, C. A. Frederick, S. J. Lippard, P. Nordlund, *Nature* **1993**, *366*, 537–543; c) E. G. Kovaleva, M. B. Neibergall, S. Chakrabarty, J. D. Lipscomb, *Acc. Chem. Res.* **2007**, *40*, 475–483; d) K. Ray, F. F. Pfaff, B. Wang, W. Nam, *J. Am. Chem. Soc.* **2014**, *136*, 13942–13958; e) J. Hohenberger, K. Ray, K. Meyer, *Nat. Commun.* **2012**, *3*, 720.

[3] a) R. G. Castillo, R. Banerjee, C. J. Allpress, G. T. Rohde, E. Bill, L. Que, J. D. Lipscomb, S. DeBeer, *J. Am. Chem. Soc.* **2017**, *139*, 18024–18033; b) G. E. Cutsail, R. Banerjee, A. Zhou, L. Que, J. D. Lipscomb, S. DeBeer, *J. Am. Chem. Soc.* **2018**, *140*, 16807–16820; c) L. Shu, J. C. Nesheim, K. Kauffmann, E. Münck, J. D. Lipscomb, L. Que, *Science* **1997**, *275*, 515–518; d) R. Banerjee, Y. Proshlyakov, J. D. Lipscomb, D. A. Proshlyakov, *Nature* **2015**, *518*, 431–434; e) A. B. Jacobs, R. Banerjee, D. E. Deweese, A. Braun, J. T. Babicz, Jr., L. B. Gee, K. D. Sutherlin, L. H. Böttger, Y. Yoda, M. Saito, S. Kitao, Y. Kobayashi, M. Seto, K. Tamasaku, J. D. Lipscomb, K. Park, E. I. Solomon, *J. Am. Chem. Soc.* **2021**, *143*, 16007–16029; f) G. T. Rohde, G. Xue, L. Que, Jr., *Faraday Discuss.* **2022**, *234*, 109–128; g) N. Mitić, L. Saleh, G. Schenk, J. M. Bollinger, Jr., E. I. Solomon, *J. Am. Chem. Soc.* **2003**, *125*, 11200–11201; h) N. Mitić, M. D. Clay, L. Saleh, J. M. Bollinger, Jr., E. I. Solomon, *J. Am. Chem. Soc.* **2007**, *129*, 9049–9065; i) P. E. Doan, M. Shanmugam, J. Stubbe, B. M. Hoffman, *J. Am. Chem. Soc.* **2015**, *137*, 15558–15566; j) R. J. Martinie, E. J. Blaesi, C. Krebs, J. M. Bollinger, Jr., A. Silakov, C. J. Pollock, *J. Am. Chem. Soc.* **2017**, *139*, 1950–1957.

[4] a) S. Friedle, E. Reisner, S. J. Lippard, *Chem. Soc. Rev.* **2010**, *39*, 2768–2779; b) E. Y. Tshuva, S. J. Lippard, *Chem. Rev.* **2004**, *104*, 987–1012; c) A. J. Jasniewski, L. Que, *Chem. Rev.* **2018**, *118*, 2554–2592; d) I. Siewert, C. Limberg, *Chem. Eur. J.* **2009**, *15*, 10316–10328; e) S. Walleck, T. P. Zimmermann, H. Hachmeister, C. Pilger, T. Huser, S. Katz, P. Hildebrandt, A. Stammler, H. Bögge, E. Bill, T. Glaser, *Nat. Commun.* **2022**, *13*, 1376.

[5] a) D. Rinaldo, D. M. Philipp, S. J. Lippard, R. A. Friesner, *J. Am. Chem. Soc.* **2007**, *129*, 3135–3147; b) W.-G. Han, L. Noodleman, *Inorg. Chim. Acta* **2008**, *361*, 973–986; c) P. E. M. Siegbahn, *Inorg. Chem.* **1999**, *38*, 2880–2889; d) T. Lovell, W.-G. Han, T. Liu, L. Noodleman, *J. Am. Chem. Soc.* **2002**, *124*, 5890–5894; e) S.-P. Huang, Y. Shiota, K. Yoshizawa, *Dalton Trans.* **2013**, *42*, 1011–1023; f) C. E. Schulz, R. G. Castillo, D. A. Pantazis, S. DeBeer, F. Neese, *J. Am. Chem. Soc.* **2021**, *143*, 6560–6577.

[6] a) N. Leidel, A. Popović-Bijelić, K. G. V. Havelius, P. Chernev, N. Voevodskaya, A. Gräslund, M. Haumann, *Biochim. Biophys. Acta Bioenerg.* **2012**, *1817*, 430–444; b) P. J. Riggs-Gelasco, L. Shu, S. Chen, D. Burdi, B. H. Huynh, L. Que, J. Stubbe, *J. Am. Chem. Soc.* **1998**, *120*, 849–860; c) L. M. K. Dassama, A. Silakov, C. M. Krest, J. C. Calixto, C. Krebs, J. M. Bollinger, M. T. Green, *J. Am. Chem. Soc.* **2013**, *135*, 16758–16761.

[7] Y. Zang, Y. Dong, L. Que, K. Kauffmann, E. Muenck, *J. Am. Chem. Soc.* **1995**, *117*, 1169–1170.

[8] H.-F. Hsu, Y. Dong, L. Shu, V. G. Young, L. Que, *J. Am. Chem. Soc.* **1999**, *121*, 5230–5237.

[9] G. Xue, D. Wang, R. De Hont, A. T. Fiedler, X. Shan, E. Munck, L. Que, Jr., *Proc. Natl. Acad. Sci. USA* **2007**, *104*, 20713–20718.

[10] a) G. Xue, A. T. Fiedler, M. Martinho, E. Münck, L. Que, *Proc. Natl. Acad. Sci. USA* **2008**, *105*, 20615–20620; b) G. Xue, R. De Hont, E. Münck, L. Que, Jr., *Nat. Chem.* **2010**, *2*, 400–405.

[11] S. K. Lee, B. G. Fox, W. A. Froland, J. D. Lipscomb, E. Munck, *J. Am. Chem. Soc.* **1993**, *115*, 6450–6451.

[12] L. Fohlmeister, K. R. Vignesh, F. Winter, B. Moubaraki, G. Rajaraman, R. Pöttgen, K. S. Murray, C. Jones, *Dalton Trans.* **2015**, *44*, 1700–1708.

[13] a) S. Kundu, F. F. Pfaff, E. Miceli, I. Zaharieva, C. Herwig, S. Yao, E. R. Farquhar, U. Kuhlmann, E. Bill, P. Hildebrandt, H. Dau, M. Driess, C. Limberg, K. Ray, *Angew. Chem. Int. Ed.* **2013**, *52*, 5622; *Angew. Chem.* **2013**, *125*, 5732; b) X. Engelmann, S. Yao, E. R. Farquhar, T. Szilvasi, U. Kuhlmann, P. Hildebrandt, M. Driess, K. Ray, *Angew. Chem. Int. Ed.* **2017**, *56*, 297; *Angew. Chem.* **2017**, *129*, 303; c) H. Stevens, P.-C. Duan, S. Dechert, F. Meyer, *J. Am. Chem. Soc.* **2020**, *142*, 6717–6728; d) S. Pfirrmann, C. Limberg, C. Herwig, R. Stößer, B. Ziemer, *Angew. Chem. Int. Ed.* **2009**, *48*, 3357–3361; *Angew. Chem.* **2009**, *121*, 3407–3411; e) S. M. Bhutto, P. L. Holland, *Eur. J. Inorg. Chem.* **2019**, 1861–1869.

[14] S. Yao, F. Meier, N. Lindenmaier, R. Rudolph, B. Blom, M. Adelhardt, J. Sutter, S. Mebs, M. Haumann, K. Meyer, M. Kaupp, M. Driess, *Angew. Chem. Int. Ed.* **2015**, *54*, 12506–12510; *Angew. Chem.* **2015**, *127*, 12686–12690.

[15] The Mössbauer spectra of **2** in powder form (Figure 1B inset) or in frozen butyronitrile solution (Figure S5B) both show a single quadrupole doublet; the minor impurity observed in molar paramagnetic susceptibility and EXAFS measurements is not detectable in Mössbauer measurements. Furthermore, comparable edge/pre-edge features of **2** in powder form and in various organic solvents (Figure S9 and Table S3) reveal that the minor impurity, the concentration of which varies in powder form and in different solvents, do not significantly affect the XAS spectra of **2**.

[16] The EPR and Mossbauer data are also consistent with $[(L)Fe^{III}O_2Fe^{II}(L^{2+})(CH_3CN)]^+$ assignments of **4**, containing low-spin Fe^{II} and high spin Fe^{III} centers (L^{2+} is the doubly oxidized β-diketiminato ligand). However, based on the XAS data, where the Fe K-edge in **4** is 0.4 eV blue-shifted relative to **2**, the possibility of the formation of any low-spin Fe^{II} ion in **4** can be excluded.

[17] Deposition Numbers 2176608 (for **2**) and 2176609 (for **3**) contain the supplementary crystallographic data for this paper. These data are provided free of charge by the joint Cambridge Crystallographic Data Centre and Fachinformationszentrum Karlsruhe Access Structures service.

Manuscript received: June 29, 2022
Accepted manuscript online: December 21, 2022
Version of record online: January 25, 2023